Supporting Information for

Directing the lithium-sulfur reaction pathway via sparingly solvating electrolytes for high energy density batteries

Chang-Wook Lee,[‡] Quan Pang,[‡] Seungbum Ha, Lei Cheng, Sang-Don Han, Kevin R. Zavadil, Kevin G. Gallagher,* Linda F. Nazar,* and Mahalingam Balasubramanian*

Corresponding Authors: mali@aps.anl.gov, kevinggallagher@gmail.com, lfnazar@uwaterloo.ca

Author Contributions: [‡] These authors contributed equally.

Experimental details

Preparation and characterization of the electrolytes

Bis(trifluoromethane-sulfonyl)imide lithium (LiTFSI), alumina (Al_2O_3), tetraethylene glycol dimethyl ether (TEGDME), tetrahydrofuran (THF), and acetonitrile (ACN) were purchased from Sigma Aldrich. 1,1,2,2-tetrafluoroethyl 2,2,3,3-tetrafluoropropyl ether (TTE) was purchased from Synquest Labs. LiTFSI was dried under vacuum overnight at 150°C. ACN and TTE were dried over alumina (activated under vacuum at ~170°C) for 24 hours to result in a water content of 0.1 and 0.6 ppm, respectively. TEGDME was dried over activated molecule sieves (4 A) for 24 hours yielding a water content of 0.6 ppm. Electrolytes were prepared in an Ar-filled glove-box with controlled moisture and oxygen level <5 ppm. The fabrication of solvate electrolyte started with a 2:1 molar ratio of ACN (or THF):LiTFSI. The mass-dictated volume of ACN (or THF) was mixed with the appropriate mass of salt and stirred at room temperature to yield a clear, viscous solution. Once clear, an equivalent volume of TTE was added and stirred to create a 50:50 mixture. For comparison, a conventional electrolyte was prepared by dissolving 1 M LiTFSI in DOL:DME (1:1, v/v) with 2 wt% of $LiNO_3$. A TEGDME solvate (G4-LiTFSI) was prepared by dissolving LiTFSI in TEGDME and TTE with a molar ratio of 1:1:4.13 The ionic conductivity was measured over a temperature range of 27-70°C in the glovebox with a 3-star conductometer (Orion) equipped with a 2-electrode epoxy conductivity probe.

Electrochemistry

Unless otherwise noted, micron-sized sulfur particles (bulk sulfur) were directly used as the active material without any special electrode architecture to avoid any unknown synergistic effect from a composite structure. Positive electrodes were cast from a slurry containing 50 wt% bulk sulfur (100 mesh, Sigma-Aldrich), 40 wt% conductive carbon (Timcal Super C45) and 10 wt% poly(vinylidene fluoride-co-hexa-fluoropropene) binder in N,N-dimethylformamide onto an aluminum current collector. Mesoporous CMK-3 carbon was synthesized following a previously reported approach.[1] KB (Ketjen Black) or CMK-3 sulfur composites were prepared by melt-diffusion of sulfur into the carbon at the desired mass ratio at 155 °C for 12 hours. The sulfur loading was fixed to 1.2 mg cm^{-2}. 2032 type coin cells were assembled in an argon-filled glovebox using a sulfur positive electrode, two sheets of 2325 CelgardTM as the separator, a Li foil negative electrode, and 10 mL gS^{-1} of electrolyte. For galvanostatic experiments, the voltage window was between 1.5 to 3.0 V vs. Li/Li^+ for 1M LiTFSI in DOL:DME (1:1) with 2% $LiNO_3$, or 1.2 to 3.0 V vs. Li/Li^+ for others (Maccor series 4400 battery tester). The same instrument was used to perform galvanostatic intermittent titration (GITT), by alternating C/10 pulses (20 min) with OCV periods (120 min). A discharge/charge rate of 1 C corresponds to a full discharge in one hour, i.e. a current of 1675 mA g^{-1}.

Material characterization

The solubility of polysulfide was measured using a UV/VIS spectrometer (Agilent 8453A). Li_2S_6 was synthesized from the reaction of sulfur and lithium superhydride following the previously reported method.[2,3] The ACN-TTE solvate (or TTE, TEGDME solvate) with saturated S_8 or Li_2S_6 at 70 °C was centrifuged and the supernatant was diluted using DOL at specific ratios for UV/VIS. Standards for calibration for each system were prepared by dissolving a known amount of the solute (S_8 or Li_2S_6) in the same mixed solvent as that for sample measurement. The SEM imaging and EDX elemental mapping were performed using a LEO 1530 field emission SEM equipped with an EDX attachment (Zeiss). Cycled cells were dissembled inside the glovebox and the recovered electrodes were thoroughly washed with DME and transferred to the SEM in Ar-filled vials.

Ohara pouch cell fabrication

The Ohara-ACN cell consists of a pouch with container laminates, positive and negative electrodes, and the separator sheets (Celgard 2325 separator). The positive and negative electrode compartments were separated by a Li^+ ion conductive glass ceramic membrane (LICGC, diameter 19 mm, thickness 150 μm, conductivity 10^{-4} S/cm at 25°C, Ohara, Japan). The Ohara glass is only permeable for Li^+ ions and serves as a diffusion barrier for liquids and gases between the two compartments. The cell assembly was performed in an argon filled glovebox. The positive electrode had a coating area of 1 cm^2, and the negative electrode had a coating area of 1.44 cm^2. Aluminum and nickel tabs (7 mm wide, 100 mm thick) were welded to the positive and the negative electrodes, respectively. The $ACN_2LiTFSI$-TTE and 1 M LiTFSI in DOL:DME electrolytes (0.2 ml each) were added by a syringe to the positive and negative electrode compartments, respectively, using a single open edge of the pouch. The final side of the pouch was heat-sealed in the vacuum sealer to help evacuate argon pockets and enhance electrode wetting by the electrolyte. A polypropylene film was placed between the top and bottom pouch container laminates to achieve effective sealing between the compartments.

Operando X-ray studies

Operando X-ray diffraction (XRD) was performed using a PANalytical Empyrean diffractometer outfitted with a PIXcel detector. The diffraction patterns were collected using Cu-Kα radiation. The patterns were collected in Bragg–Brentano geometry. The cell was cycled at C/30 rate with a pattern collection time of 15 mins (20-55°). Patterns were group-merged by three for phase quantification. The Li_2S, α-S and β-S phases were quantified by integrating the peak area of their corresponding major peaks, (022), (222) and (200), respectively. The cathodes were prepared from sulfur, hand-ground with 30 wt% Ketjen black carbon.

Also, sulfur K-edge operando X-ray absorption near edge measurements (XANES) were carried out at beamline 9-BM-B in the Advanced Photon Source. The operando XANES (X-ray absorption near edge structure) study was carried out at the sector 9-BM-B in the Advanced Photon Source using a Si (111) crystal monochromator. The instrumental resolution in the energy range near the sulfur K-edge is about 0.35 eV, with a beam size of about 200 ×200 μm. All of the XANES studies were carried out under constant helium flow in the sample chamber and the data were collected in fluorescence mode using a 4-element vortex detector. Energy calibration was carried out using sodium thiosulfate pentahydrate, with a pre-edge feature at 2469.2 eV. The cell used to perform operando XANES was adapted from the 2032 coin cells using an aluminized Kapton™ window. Other modifications were limited to the electrode design: 50% of bulk sulfur was mixed with 40% of conductive carbon and 10% of PVDF to reach 50 wt.% sulfur and cast onto carbon paper (AvCarb P50, Ballard Material Products).

List of Supplementary Figures/Tables

Table S1. Factors used to calculate the estimated limits for the electrolyte/sulfur ratio in cells (see main text).

| Property	Value	Units			
Electrode mass fractions			crystal density		
Sulfur	0.5	$g/g_{electrode}$	2	g/cm^3	
Carbon black	0.4	$g/g_{electrode}$	1.8	g/cm^3	C45
Binder	0.1	$g/g_{electrode}$	1.78	g/cm^3	PVDF
Electrode mass loading	2.5	$mg_{electrode}/cm^2$			
Electrode sulfur loading	1.25	mg_S/cm^2			
Electrode thickness	50	um			
Electrode porosity	0.74	cm^3/cm^3			
Separator thickness	50	um			
Separator porosity	0.4	cm^3/cm^3			
Separator area	2.01	cm^2			
Positive electrode area	1.54	cm^2			
Available porosity in cell	0.0097	cm^3			
Minimum E/S Ratio	**5.0**	**$mL_{electrolyte}/g_S$**	For cell construction		
Electrode local E/S Ratio	2.9	$mL_{electrolyte}/g_S$	For performance considerations only		
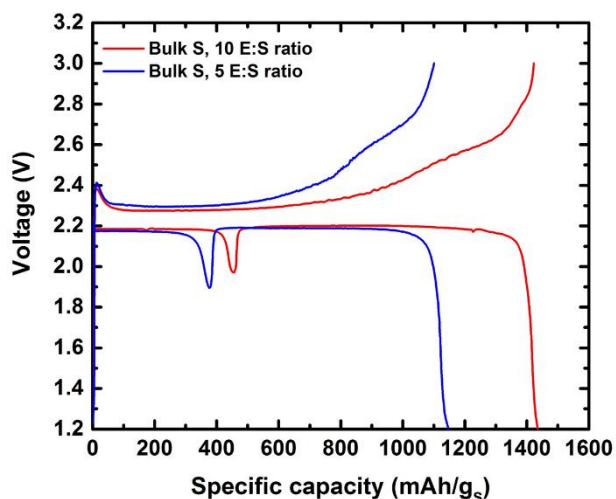
Fig. S1. Comparison of the first cycle voltage profiles at a C/30 rate on halving the electrolyte volume/sulfur ratio. Shown in red is the profile for 10 mL g_s^{-1} (as described in the main text), and in blue for 5 mL g_s^{-1}.
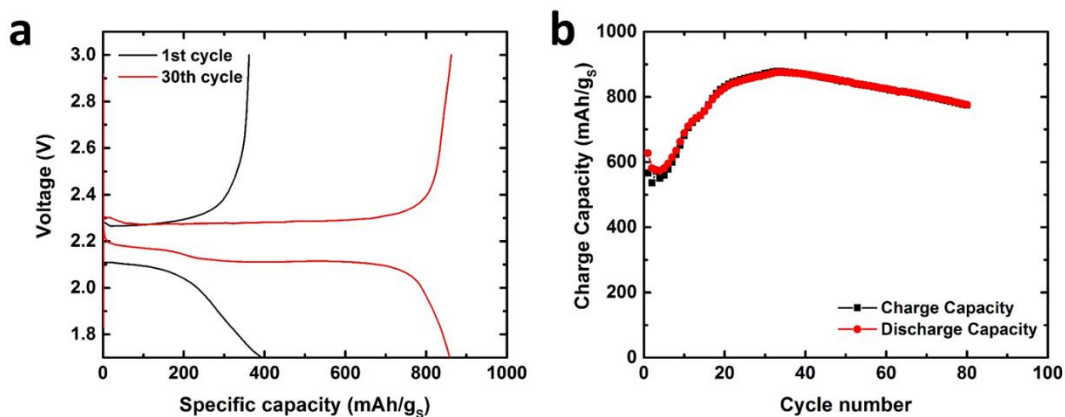

4

Figure S2. Electrochemical performance of the Ohara-ACN cell *(a) voltage profile of the first cycle and 30th cycle at a rate of C/10 and (b) cycling performance over 80 cycles.*
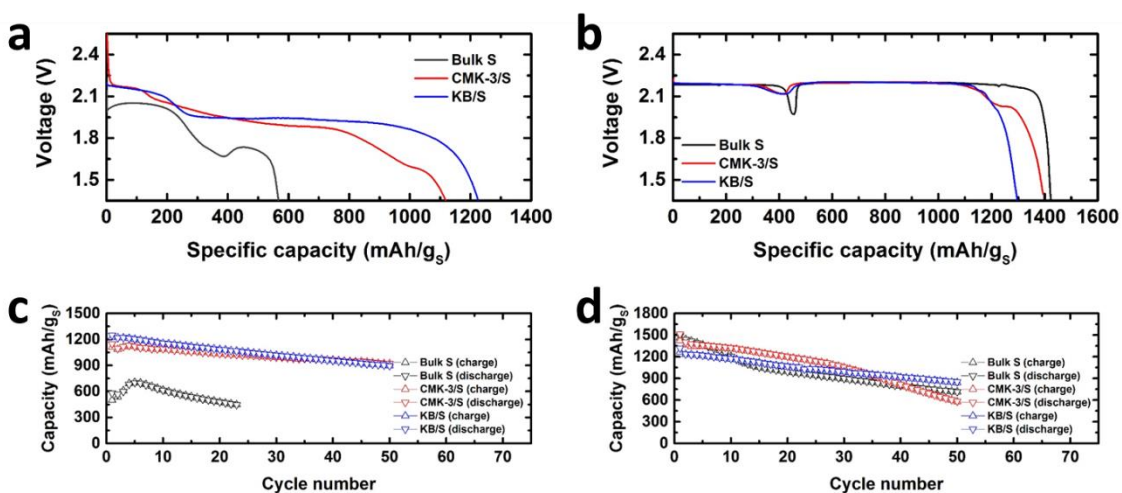

Figure S3. Electrochemical performance of bulk S, CMK-3/S and the KB/S nanocomposite. *(a) Voltage profile of the first cycle at a C/30 rate at (a) 30°C and (b) 55°C. Cycling performance over 50 cycles at (c) 30°C and (d) 55°C.*
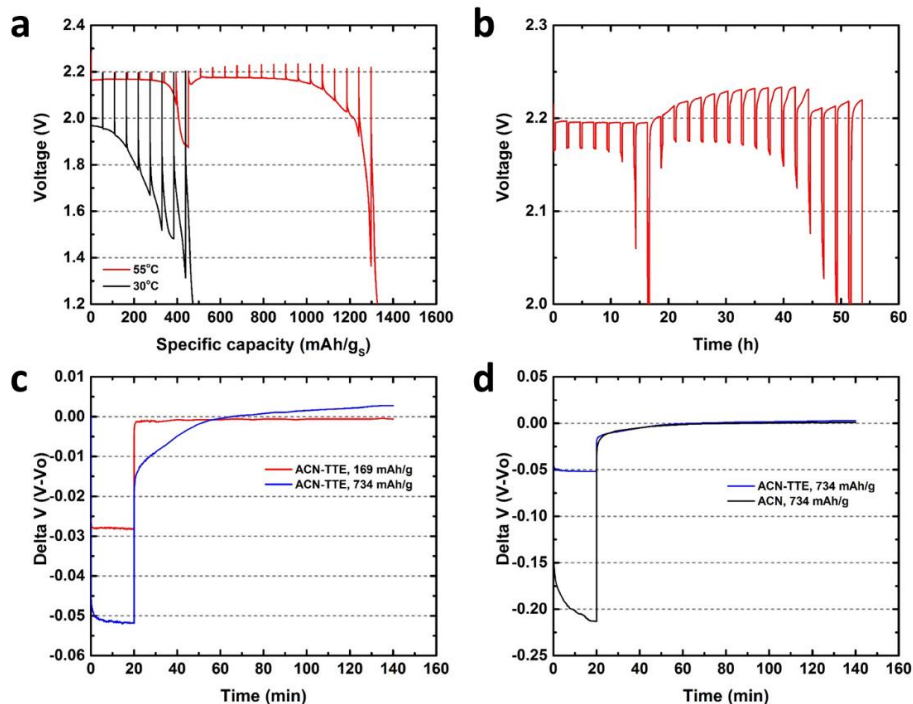

Figure S4. GITT (galvanostatic intermittent titration technique) dynamics difference for bulk sulfur electrodes. *(a) Comparison of GITT curves at 30˚C and 55˚C and (b) polarization relaxation (i.e. kinetic) behaviour at 55˚C, (c) as a function of SOC with ACN$_2$LiTFSI-TTE, (d) comparison of ACN$_2$LiTFSI vs ACN$_2$LiTFSI-TTE at 55˚C in the second plateau region.*

Discussion of Figure S4. In the region before the dip, the quasi-equilibrium voltage attains a constant value of 2.20 V both at 30°C and 55°C as shown in **Figure S4a**. As discharge progresses and traverses the dip, the OCV actually increases. The unique dip is also not observed in the equilibrium voltage profile, suggesting it is kinetically controlled. Though the discharge finished immediately thereafter due to the slow kinetics at 30°C, the overall reaction mechanism is clearly maintained at all temperatures examined here. Inspection of the voltage relaxation profiles at 55°C shown in **Figure S4b** reveals that the overpotential is small during the initial 400 mAh g_s^{-1} of capacity and that the relaxation time used (the GITT "rest" period) is sufficient for the system to reach quasi-equilibrium. Furthermore, the voltage response resembles that of a single resistor with little temporal variation.

The quasi equilibrium voltage response is complex in the region past the dip – the OCV shows a small, continuous increase in the range of 400-1000 mAh g_s^{-1}, followed by a small reduction of the OCV towards the end of discharge. The complexity of the reactions in the region past the dip becomes clearer when GITT dynamics are plotted as a function of state-of-charge and time (**Figure S4c** and **S4d**). GITT dynamics comparing ACN$_2$LiTFSI vs ACN$_2$LiTFSI-TTE at 55°C in the second plateau region are shown in **Figure S4d**. While the overpotential of ACN$_2$LiTFSI at 734 mAh g_s^{-1} is ~ 200 mV, much larger than that in ACN$_2$LiTFSI-TTE, the equilibrium voltage is the same in both cases. Before the dip (e.g. at 169 mAh g_s^{-1}), the observed polarization is only 28 mV, demonstrating fast electrode kinetics in this region. For the plateau after the dip (e.g. at 734 mAh g_s^{-1}), the polarization doubled in magnitude to 50 mV and did not reach equilibrium in the allotted rest time. In conventional Li-S electrochemistry, with DOL:DME electrolyte, the "knee" that appears about a quarter of the way into discharge is associated with the nucleation of solid products and initiates the progressive reduction of soluble polysulfides to insoluble solid precipitates. As the reaction in the ACN-TTE cell during initial discharge does not correspond to the conversion of S_8 to long-chain polysulfides, the reaction as the dip is traversed cannot be ascribed simply to a reduction of soluble polysulfides to insoluble Li$_2$S.
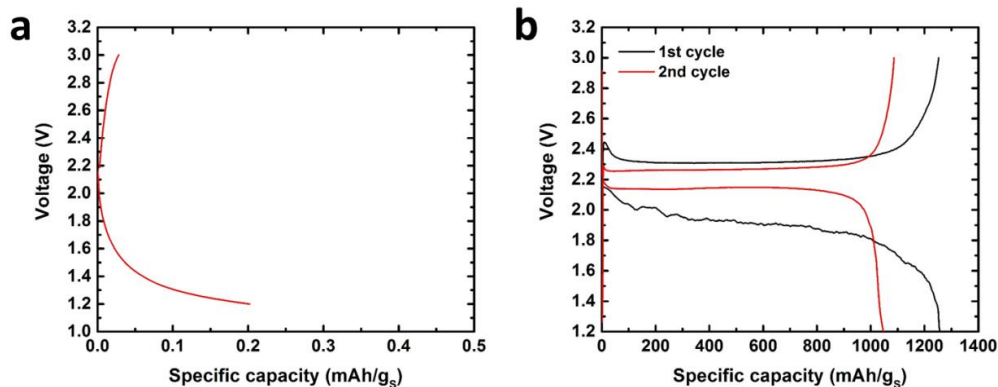
Figure S5. Electrochemical performance of bulk S in ACN₂LiTFSI at C/30. Voltage profile of the (a) first cycle at 30˚C and (b) first and second cycle at 55˚C.

Discussion of Figure S5. To investigate how much the new Li-S cell reaction is affected by addition of TTE, the sulfur electrode was examined in the solvate $ACN_2LiTFSI$ electrolyte without TTE. In this electrolyte, the bulk sulfur electrode has almost no capacity at 30°C, which we ascribe to a high electrolyte viscosity that may prevent adequate wetting of the electrode. In sharp contrast, the same system at 55°C shows a reasonably high capacity of ~1000 mAh g_s^{-1}, but an unstable first discharge profile, and poor reversible capacity and cycle life that are also likely due to the high viscosity.
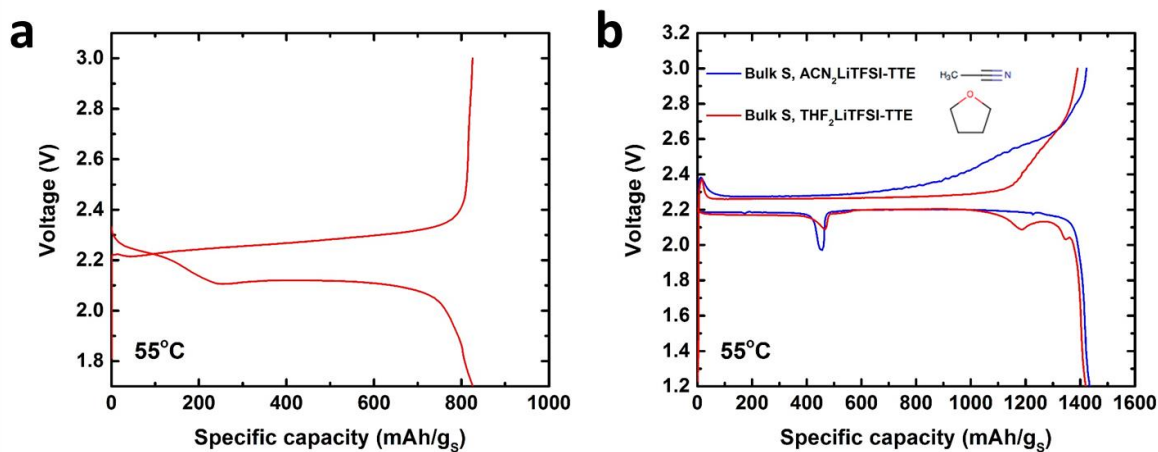

Figure S6. First cycle voltage profile during galvanostatic cycling at 55•C. (a) using 1M LiTFSI in acetonitrile in the positive electrode compartment of a cell with Ohara glass membrane at a C/10 rate and (b) comparison of different solvate electrolytes at a C/30 rate (1C capacity = 1675 mAh/gₛ).

Discussion of Figure S6. **Figure S6a** shows that the Li-S electrochemistry in 1M LiTFSI in ACN, using a cell with an Ohara glass membrane, matches that observed in other fully solvating systems such as DOL:DME. However, the Li-S electrochemistry measured in $THF_2LiTFSI$-TTE closely resembled that of the ACN-TTE electrolyte (**Figure S6b**). These electrolytes have a compact primary solvent molecule that has a single functional group in common which exhibits only moderate binding energy to Li+ cations.[4] By demonstrating that both THF and ACN solvates support this new Li-S electrochemistry, we propose that several new electrolyte systems likely still exist to explored to examine structure-property relationships.
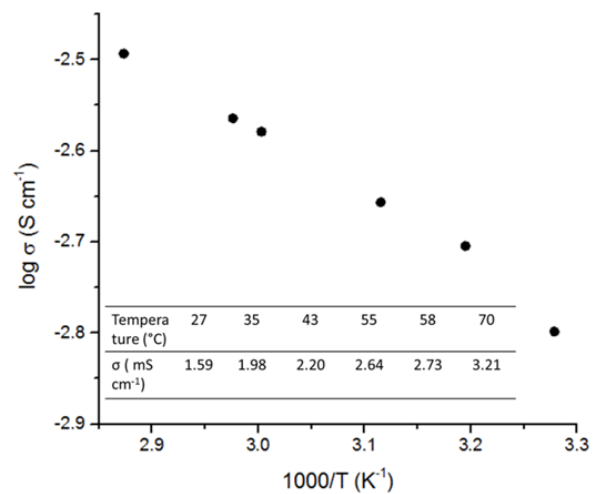
Temperature (°C)	27	35	43	55	58	70
σ (mS cm⁻¹)	1.59	1.98	2.20	2.64	2.73	3.21

Figure S7. Ionic conductivity of ACN₂-LiTFSI-TTE electrolyte at various temperatures.
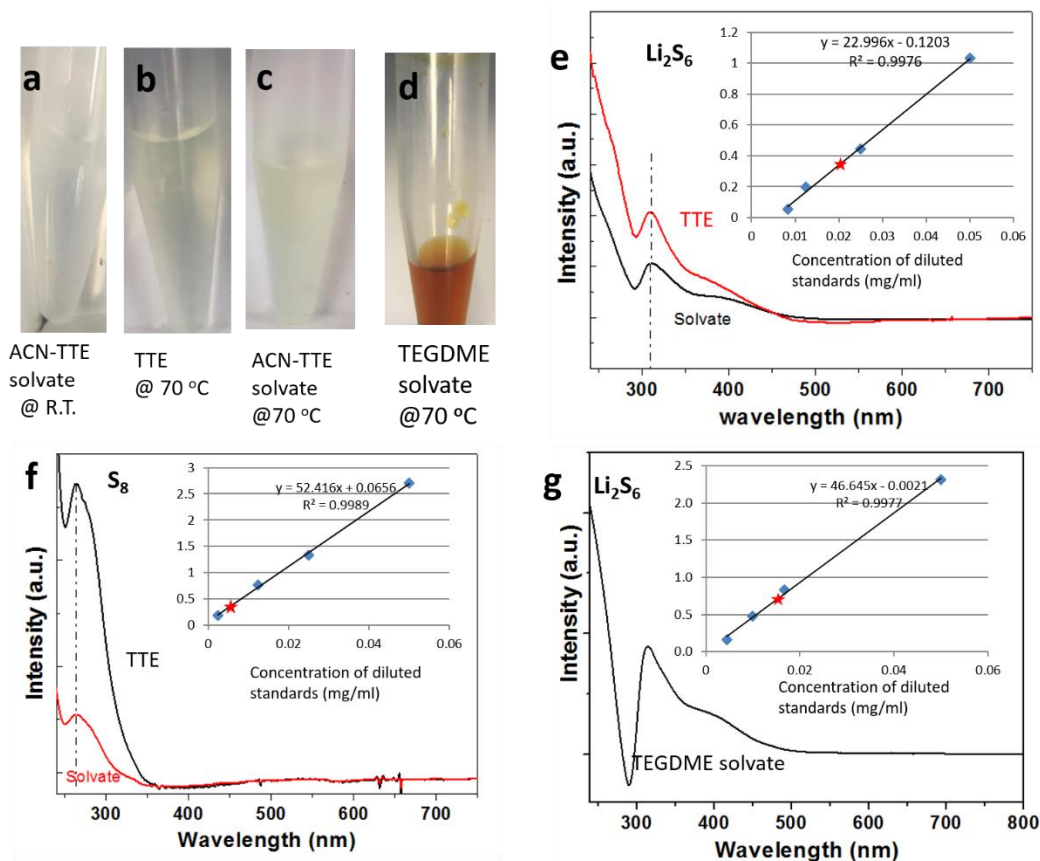

Figure S8. Polysulfide solubility measurement. *Visual confirmation of polysulfide solubility in (a) ACN solvate at R.T. (b) TTE at 70˚C (c) ACN-TTE solvate at 70˚C and (d) TEGDME solvate at 70˚C. Representative UV-vis spectra of (e) Li_2S_6 and (f) S_8 in ACN-TTE solvate and TTE and (g) Li_2S_6 in TEGDME solvate; insets are the representative calibration curves for Li_2S_6 in ACN solvate (e), S_8 in ACN solvate, (g) Li_2S_6 in TEGDME solvate.*

Discussion of Figure S8.   The images (**Figure S8a-d**) were taken after the cooling the saturated hot solutions with the respective solutes to room temperature for 1 day. The R.T. saturated ACN solvate is colorless, while the 70˚C saturated TTE and ACN solvate is pale yellow. For UV-vis spectroscopy, the supernatant of the S_8 or Li_2S_6 saturated solutions (in TTE, the ACN solvate or TEGDME solvate) was diluted with DOL in a certain ratio (e.g. 20 times diluted for S_8 in TTE). For calibration, the standards for measurement of each respective system were prepared by dissolving a known amount of S_8 or Li_2S_6 in DOL, mixed with the same ratio of the respective solution as that for the sample preparation, for higher accuracy. In all cases, the peak intensity of standards (at ca. 315 nm for Li_2S_6 and 265 nm for S_8) shows a linear relationship with respect to the concentration of solutes, in a range that includes the sample to be measured (marked as the red asterisks).
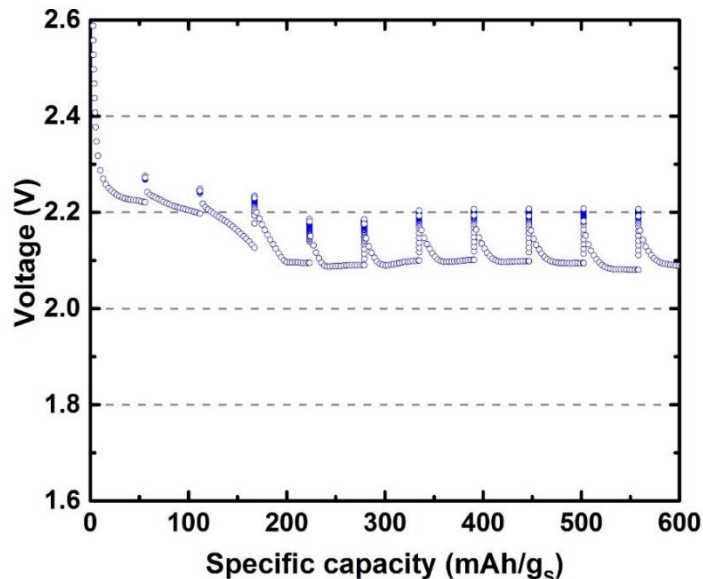
Figure S9. GITT** (galvanostatic intermittent titration technique) **profile using the TEGDME solvate showing the OCV response in the first plateau.
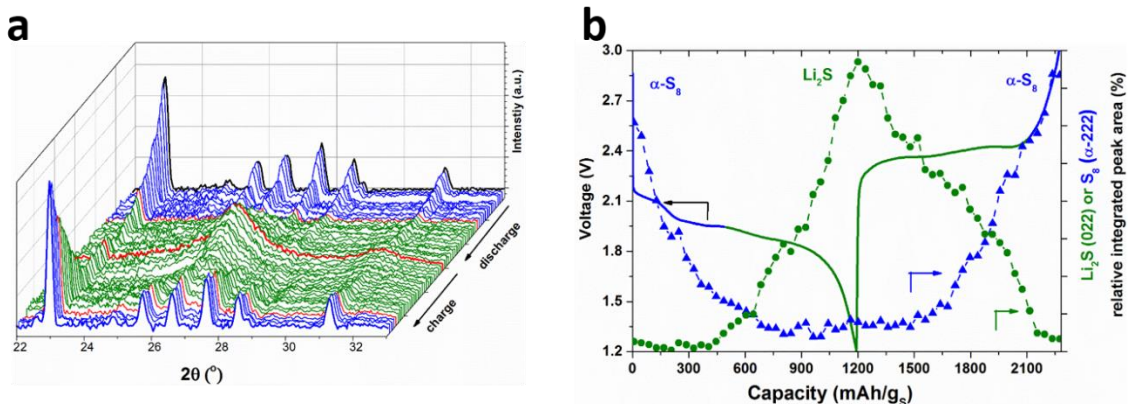

***Figure S10. Operando XRD** (X-ray diffraction) **of ACN-TTE solvate at RT.** (a) The waterfall plots showing the evolution of XRD patterns (22-33°) obtained operando as a function of discharge/charge states and (b) the peak-area quantified evolution of crystalline sulfur (α-S$_8$, blue dotted lines) and Li$_2$S (green dotted lines) phases as a function of the capacity, during 1st full cycle for the cell in the ACN-TTE solvate electrolyte at room temperature. The red pattern in the center of (a) indicates the end of discharge.*

Discussion of Figure S10. The sulfur speciation for the ACN-TTE cell at room temperature shows the same trend as that at elevated temperature, 70°C. Specifically, the α-S$_8$ is consumed slowly and does not reach minimum until the end of the second plateau. The α-S$_8$ phase, instead of β-S$_8$, is formed upon charge, and at a much earlier stage than that in DOL:DME cell. Note that there is a small percentage of α-S$_8$ remaining even at the end of discharge, due to the limited kinetics at room temperature. The crystalline Li$_2$S starts forming right before the second plateau and experiences a linear increase and decrease upon discharge and charge respectively.
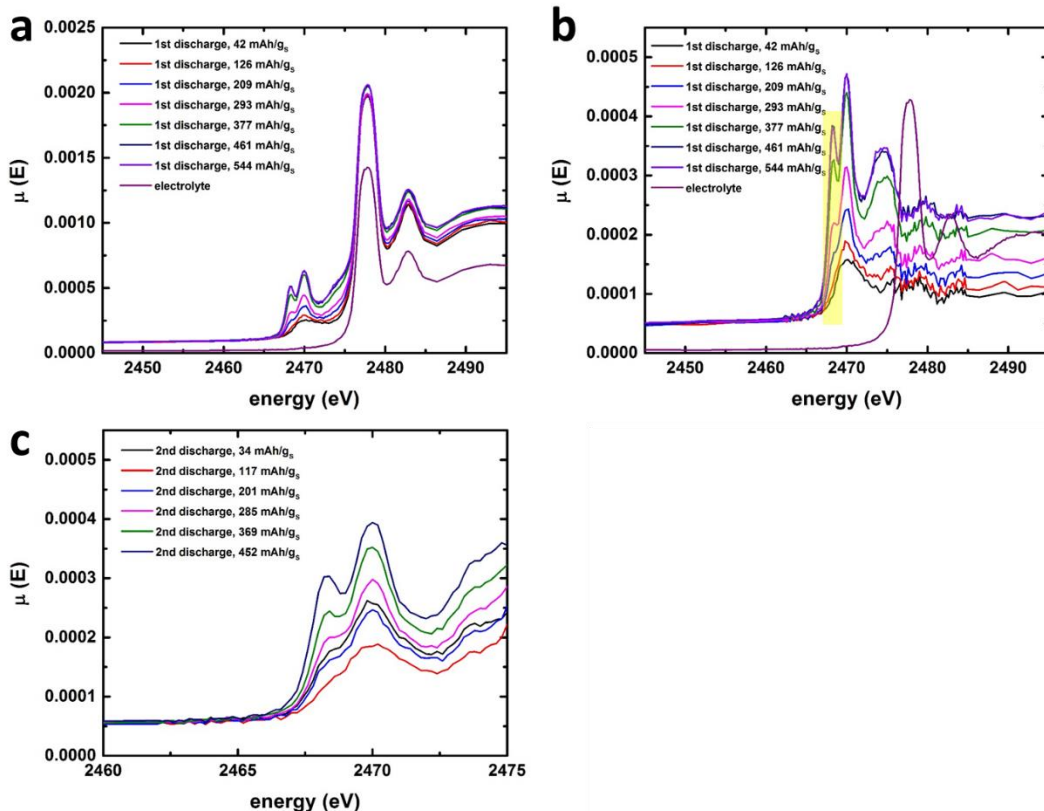
Figure S11. Operando XANES (X-ray Absorption Near Edge Spectroscopy). *(a) raw XANES curves prior to the 'dip' at first discharge (b) the unnormalized raw XANES curves after subtraction of the sulfur electrolyte signal and (c) XANES curves during second discharge with an ACN-TTE cell that uses bulk sulfur electrodes at 60 ^{o}C*

Discussion of Fig S11. **Figure S11a** shows the operando, first discharge, raw XAS data from experiments performed at 60°C to monitor the sulfur speciation in ACN-TTE cell in the region prior to the 'dip'. Recall that XRD studies show a reduction in intensity of crystalline α-S_8 peaks but no new crystalline phase is evidenced prior to the 'dip'. Sulfur XAS studies of this system suffers from two main complications: 1) the solvate electrolyte contains a significant amount of sulfur from TFSI- that contributes a large parasitic background signal. This signal was subtracted (see below) but is a source for systematic errors; 2) sulfur in the electrode is present as micrometric particles and the loading is very high. This causes severe, non-linear, self-absorption distortions of the XAS signal. Thus the spectra differ from those earlier reported for nanometric-sized sulfur.[4] The amount of distortion seen for sulfur in the starting electrode is consistent with that expected for ca. 2 μm sulfur particles, gauged by comparing to the work of Pickering et al.[3] We note that distortions will be minimized if the thickness of the particles is below 200 nm.[2, 4]

Figure S11b illustrates the unnormalized raw data after subtraction of the sulfur electrolyte signal. For comparison, a scaled signal of the electrolyte is also shown. Note that little or no residue from the strong 'white line' feature of the TFSI- electrolyte at ca. 2477.7 eV is seen; this shows that the subtraction is largely successful. Onset of discharge leads to significant changes in the sulfur signal and careful inspection of the spectral evolution in the extracted data reveals the following salient points: (1) A pre-edge peak at ca. 2468.25, highlighted by the yellow box, is seen early in discharge and grows significantly as discharge progresses. The presence of this pre-edge peak is unequivocal evidence for the generation of polysulfide

dianion species.[3, 6-8] Given the low solubility of polysulfides in the electrolyte (**Table 1**), we ascribe the pre-edge signal to an amorphous or poorly crystalline polysulfide species. (Such species would contribute to the observed XAS signal but will not create new peaks in the operando diffraction.); (2) trisulfur radicals are known to exhibit a characteristic feature ca. 2 eV lower than that seen for dianions; the absence of a clearly observable feature in that region in **Figure S11b** indicates that trisulfur radicals, if present, are below the detection limit[9-11]; (3) the increase in pre-edge intensity is accompanied with the development of another relatively sharp feature at ca. 2474.75 eV.[5, 7, 11-13] Such a feature is not seen for long-chain polysulfides and therefore provides circumstantial evidence for the presence of medium-to-short chain polysulfides, Li_2S_x (x<4); and (4) there is an apparent increase in the sulfur signal level that manifests as a significant increase in the overall background well past the edge.[3] When this data set is normalized using routine XAS data analysis procedures, the relative edge-jump appears to increase.

This observation—the apparent increase in edge jump—is likely a direct consequence of the complexity introduced by the non-linear distortion from self-absorption effects coupled with the morphology/location of the deposited product on the electrode. Self-absorption heavily suppresses feature with high absorption relative to those with low absorption in a rather non-linear fashion. This leads to a significant reduction in the intensity of the bulk sulfur white line and also distorts and lowers the effective sulfur K-edge jump. If the product particles that are formed are thin (of the order of 200 nm or lower), and if they either coat the original bulk sulfur particles or distribute themselves as plates on the electrode surface, the sulfur XAS signal from the product phase will suffer smaller self-absorption distortions. However, SEM images (see next page) suggest that the products phase does not distribute uniformly on the entire electrode surface for the ACN/TTE solvate system. Therefore, we suggest that the apparent increase in edge jump has its origin in the intricate details of product formation, morphology, and distribution. The SEM and XAS findings, taken together, point to the possible growth of a thin shell of products on the original sulfur particles as the sulfur is consumed during discharge.

The overall spectral evolution is reminiscent of that obtained in the previous room temperature XAS study.[3] That study used melt-diffused sulfur electrodes wherein the sulfur is homogeneously distributed with a much smaller primary sulfur particle size. Self-absorption, though present, manifests differently in that study. For completeness, we show in **Figure S11c**, the data obtained during second discharge with an ACN-TTE cell that uses bulk sulfur electrodes at 60°C. The spectral evolution is very similar to that seen during first discharge.
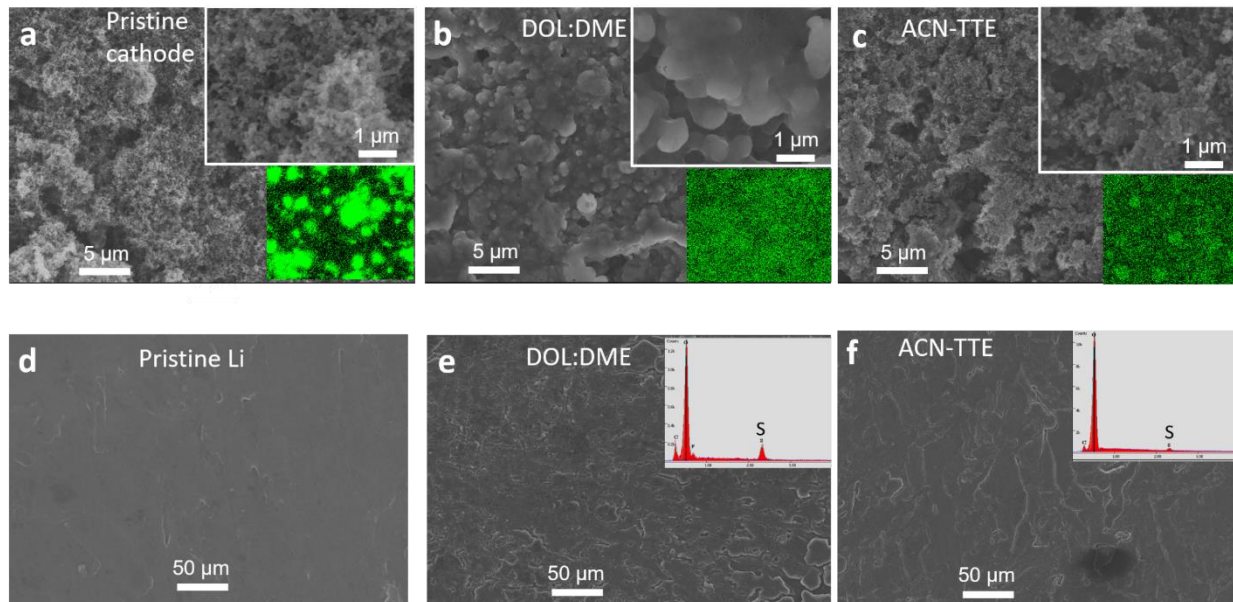
Figure S12. Ex-situ SEM images and EDX of the bulk S cathodes and Li metal anodes at different states*. (a-c) The SEM images (and enlarged, insets) and the EDX sulfur mapping (insets) of (a) pristine cathodes, cathodes after 1ˢᵗ discharge in (b) DOL:DME and (c) ACN-TTE solvate electrolytes. (d-f) The SEM images and EDX spectra (emphasizing the S signal) of the pristine Li and Li anodes after 1ˢᵗ full cycle in (e) DOL:DME and (f) ACN-TTE solvate electrolytes. Cells were cycled at 55°C and C/30.*

Discussion of Figure S12. Ex-situ SEM studies were used to image the cathode surface morphology after first discharge and the sulfur elemental distribution on Li anodes after a full cycle. The EDX mapping of the pristine cathode shows the presence of bulk sulfur as micron-sized particles (**Figure S12a**). After the first discharge, the cathode run in DOL:DME shows an agglomerated layer of the discharge product (Li_2S) on the surface facing the electrolyte (**Figure S12b**). This is the direct consequence of the high solubility of polysulfides. However, the cathode run in the ACN-TTE electrolyte preserves the morphology of the pristine electrode without any signs of a agglomerated Li_2S layer (**Figure S12c**). The EDX sulfur mapping in the ACN-TTE system shows that the sulfur particles remain as distributed as in the pristine electrode, although a small reduction in the particle size compared to the pristine electrode cannot be ruled out. The Li metal anode surface was also examined after one full cycle. The pristine Li anode has a clean surface (**Figure S12d**). The Li anodes in the DOL:DME electrolyte show a rough surface with a porous layer, in contrast to the smooth surface exhibited for the ACN-TTE electrolyte (**Figure S12e** and **S12f**). Furthermore, a factor of ten less sulfur was found compared to the DOL:DME cell (ca. 0.4 at.% vs 3.8 at.%), as determined by EDX spectra (inset **Figure S12e** and **12f**, **Figure S13**). This suggests a quasi-solid-state reaction with only minimal polysulfide shuttling.
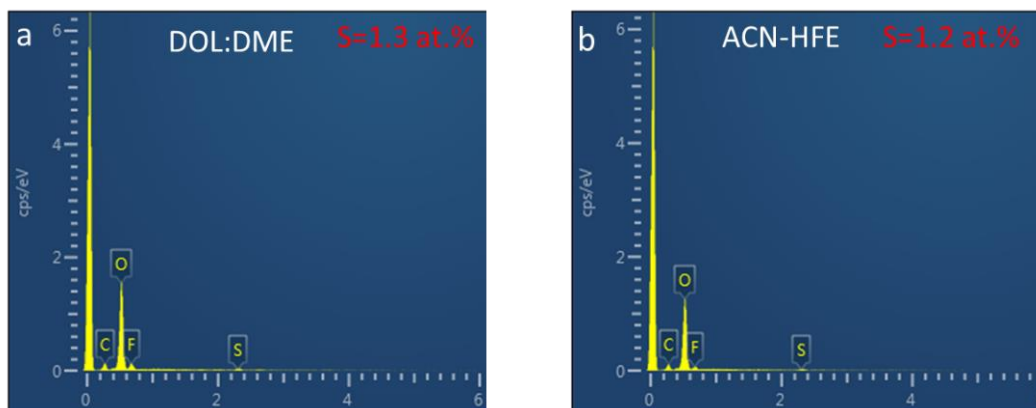
Figure S13. EDX spectra of Li/Li symmetric cells. EDX spectra in (a) DOL:DME and (b) ACN-TTE electrolytes, after one full cycle using the same current density, discharge/charge capacity and temperature (55 °C), respectively, as those for SEM/EDX studies shown in Figure S12e,f.

Discussion of Figure S13. The sulfur element on the Li anode surface comes from two sources: the reaction of cross-over polysulfides with Li metal, and the decomposition of LiTFSI salt. In **Figure S12e** and **f**, we see that the sulfur element percentage is 5.1% and 1.6 at.% for DOL:DME and ACN-TTE, respectively. Here in the symmetric cells, the percentage of sulfur, which comes only from LiTFSI decomposition, is 1.3 at.% and 1.2 at.% for DOL:DME and ACN-TTE, respectively. Therefore, a back-of-the-envelope calculation of the percentage of sulfur from the polysulfide shuttling is 3.8 at.% and 0.4 at.% for DOL:DME and ACN-TTE, respectively.
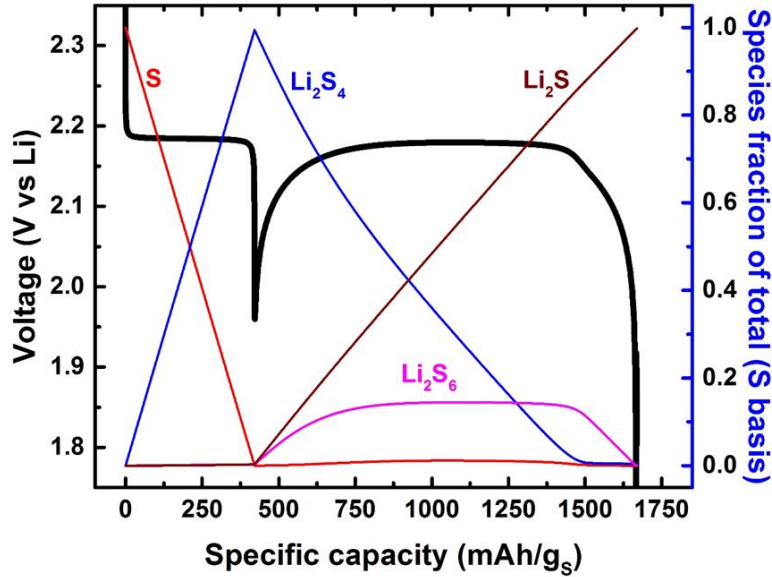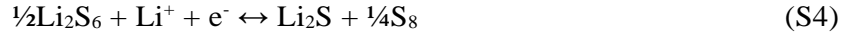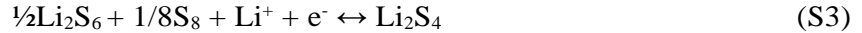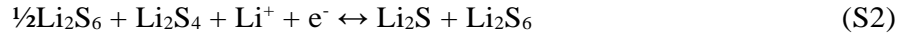
Figure S14. Kinetic model. *An increase in k₄ by 50% modifies the model response by simulating a voltage curve to be nearly of the same potential before and after the curve; thus less elemental sulfur is produced during the latter two-thirds of discharge.*

We developed a mathematical model to represent the kinetics of the reaction occurring in the cathode. Clearly more work is needed for definitive proof of chemical speciation; however, we believe the following reaction sequence on discharge is supported by the work presented herein. We attempt to remain as general as possible in our assertions, but precise speciation is required in order to balance stoichiometry. This model allows us to identify key processes responsible for the electrochemical characteristics of the unique electrochemistry observed in the ACN-TTE electrolyte. To minimize the number of unknowns and the number of parameters to be calibrated, we have assumed that Li_2S_3 undergoes rapid chemical reaction via the stated **Eqs 3-5** in the main text. We have recast **Eqs 1-5** as the following four electrochemical reactions **S1-S4**.

$$\tfrac{1}{2}S_8 + 2Li^+ + 2e^- \leftrightarrow Li_2S_4 \tag{S1}$$

$$\tfrac{1}{2}Li_2S_6 + Li_2S_4 + Li^+ + e^- \leftrightarrow Li_2S + Li_2S_6 \tag{S2}$$

$$\tfrac{1}{2}Li_2S_6 + 1/8S_8 + Li^+ + e^- \leftrightarrow Li_2S_4 \tag{S3}$$

$$\tfrac{1}{2}Li_2S_6 + Li^+ + e^- \leftrightarrow Li_2S + \tfrac{1}{4}S_8 \tag{S4}$$

We propose the following rate expressions in **S5-S8** for **S1-S4**. The standard potentials, U^o, for **S6-S8** are set equivalent due to the proposed mechanism in the main text. We note that the proposed reaction mechanism is not symmetrically reversible owing to disproportionation, as shown by the operando XRD.

$$r_1 = \frac{i_1}{n_1F} = k_1\left[\theta_{Li2S4}\exp\left(\frac{\alpha F}{RT}(V - U_1^o)\right) - \theta_{S8}\exp\left(-\frac{\alpha F}{RT}(V - U_1^o)\right)\right] \tag{S5}$$

$$r_2 = \frac{i_2}{n_2 F} = k_2 \left[\theta_{Li2S} \frac{C_{Li2S6}}{C_{Li2S6,0}} \exp\left(\frac{\alpha F}{RT}(V - U_2^o)\right) - \theta_{Li2S4} \left(\frac{C_{Li2S6}}{C_{Li2S6,0}}\right)^{1/2} \exp\left(-\frac{\alpha F}{RT}(V - U_2^o)\right) \right] \quad (S6)$$

$$r_3 = \frac{i_3}{n_3 F} = k_3 \left[\theta_{Li2S4} \exp\left(\frac{\alpha F}{RT}(V - U_3^o)\right) - \theta_{S8} \left(\frac{C_{Li2S6}}{C_{Li2S6,0}}\right)^{1/2} \exp\left(-\frac{\alpha F}{RT}(V - U_3^o)\right) \right] \quad (S7)$$

$$r_4 = \frac{i_4}{n_4 F} = k_4 \left[\theta_{S8} \theta_{Li2S} \exp\left(\frac{\alpha F}{RT}(V - U_4^o)\right) - \left(\frac{C_{Li2S6}}{C_{Li2S6,0}}\right)^{1/2} \exp\left(-\frac{\alpha F}{RT}(V - U_4^o)\right) \right] \quad (S8)$$

Here, F is Faraday's constant of 96,485.3 C mol⁻¹, R is the universal gas constant of 8.31447 J mol⁻¹ K⁻¹, and T is the temperature of 328 K. All transfer coefficients, α, are assumed to equal to 0.5. The reactants appear in the rate equations **S5-S8** in two different ways. The first is in the classical approach where a species concentration is normalized to a reference value as is the case for Li_2S_6. In the model, the ratio of concentrations is replaced with a molar ratio of moles of the species, N_{Li2S6}, and total molar S quantity available to eliminate the volume of electrolyte from simulation. Li_2S_6 has been measured to have a finite solubility in the ACN-TTE electrolyte as reported in the main text. However, amorphous, solid-state Li_2S_6 also exists. There is likely only a small quantity of the Li_2S_6 dissolved in the electrolyte, meaning the majority of the Li_2S_6 estimated by the model would reside in the solid state. Future work will aim to quantify the relative fractions of solid species versus solution species.

The second reactant formulism invokes a species specific factor, θ_j, which is used to represent the species that occur primarily in the solid state. A Langmuir isotherm is used to scale the species j as a function of its molar sulfur fraction of the total sulfur content, ω_j. Here, $\omega_j = N_j/N_{S,total}$. K is an equilibrium constant for the isotherm.

$$\theta_j = \frac{K\omega_j}{1+K\omega_j} \quad (S9)$$

The plateau observed in the first third of discharge likely represents a classical two phase reaction. While some indication exists to suggest this reaction takes place in the solid state, we do not yet have definitive evidence. To simulate this behavior, we use a Langmuir isotherm with a large-valued equilibrium constant to represent the reactants which may be solid species in the rate equation. To be clear, all species except for the soluble polysulfide Li_2S_6 are treated with the isotherm. The physical meaning of this expression in this reaction is unclear, but the mathematical formalism provides the following advantage. For solid materials that are invariant in composition, the activity of the phase is taken as unity. Thus the electrochemical potential of a chemical transformation of sulfur to a solid intermediate chain length polysulfide such as Li_2S_4 would be invariant during the majority of the reaction as the activities of the reactant and product are also invariant (i.e. unity). In the rate expression, the ability of the reaction to progress relies upon the presence of some finite quantity of the reactant and the key physical attribute that relates to the mechanism (e.g. surface area, triple phase boundary length, etc). As the quantities of these key physical attributes are unknown, we use the Langmuir isotherm expression to provide a representation of the unit activity for most quantities of reactant but a reaction rate that tends to zero as the material is exhausted.

Materials balance equations for all species are:

$$\frac{\partial N_{S8}}{\partial t} = \frac{1}{2}r_1 + \frac{1}{8}r_3 - \frac{1}{4}r_4 \tag{S10}$$

$$\frac{\partial N_{Li2S4}}{\partial t} = -r_1 + r_2 - r_3 \tag{S11}$$

$$\frac{\partial N_{Li2S6}}{\partial t} = -\frac{1}{2}r_2 + \frac{1}{2}r_3 + \frac{1}{2}r_4 \tag{S12}$$

$$\frac{\partial N_{Li2S}}{\partial t} = -r_2 - r_4 \tag{S13}$$

The simulation is run under galvanostatic conditions to maintain total current, I, with balance of

$$I = i_1 + i_2 + i_3 + i_4 \tag{S14}$$

until the electrode voltage was calculated below a lower cutoff, typically 1.7 V. The electrode is simulated with 1 mg of sulfur per cm^2 at the C/30 rate, where C is the theoretical specific capacity of 1675 mAh per g. No estimation of specific interfacial area is made and thus all parameter values refer to current collector area. Values of all other parameters are reported in **Table S2**. The standard potential for reactions 2-4 is best fit with values near 2.4 V vs Li in contrast to the experimental approximation of an equilibrium potential of 2.3 or even 2.25 V vs Li reported in the main text. The slow relaxation of the mixed potential in the experiment makes a precise determination of standard potential challenging with the current mechanistic understanding. The parameter estimation of $U^o_{2\text{-}4}$ is also confounded by the simplified treatment of solution species and the absence of mass transfer effects.

Table S2. Parameter values used in the numerical model.

Parameter	Units	Value
k_1	mmol cm^{-2} s^{-1}	5.2×10^{-7}
k_2	mmol cm^{-2} s^{-1}	7.2×10^{-8}
k_3	mmol cm^{-2} s^{-1}	1×10^{-7}
k_4	mmol cm^{-2} s^{-1}	4.1×10^{-8}
K		100
U^o_1	V vs Li/Li$^+$	2.2
U^o_2, U^o_3, U^o_4	V vs Li/Li$^+$	2.4
n_1	-	2
n_2, n_3, n_4	-	1

References

1.   Ji, X.; Lee, K. T.; Nazar, L. F., A highly ordered nanostructured carbon-sulfur cathode for lithium-sulfur batteries. *Nat. Mater.* **2009**, 8, 500-506.
2.   Gladysz, J. A.; Wong, V. K.; Jick, B. S., Introduction of sulfur into organic molecules via lithium triethylborohydride reduc-tion of S8. J. Chem. Soc., *Chem. Commun*. 1978, 838-839.
3.   Cuisinier, M.; Cabelguen, P.-E.; Evers, S.; He, G.; Kolbeck, M.; Garsuch, A.; Bolin, T.; Balasubramanian, M.; Nazar, L. F., Sulfur Speciation in Li–S Batteries Determined by Operando X-ray Absorption Spectroscopy. *J. Phys. Chem. Lett*. 2013, 4, 3227-3232.
4.   Okoshi, M.; Yamada, Y.; Yamada, A.; Nakai, H., Theoretical Analysis on De-Solvation of Lithium, Sodium, and Magnesium Cations to Organic Electrolyte Solvents. *J. Electrochem. Soc.* **2013**, 160, A2160-A2165.
5.   Pickering, I. J.; George, G. N.; Yu, E. Y.; Brune, D. C.; Tuschak, C.; Overmann, J.; Beatty, J. T.; Prince, R. C., Analysis of Sulfur Biochemistry of Sulfur Bacteria Using X-ray Absorption Spectroscopy. *Biochemistry*, **2001**, 40, 8138-8145.
6.   Wujcik, K. H.; Velasco-Velez, J.; Wu, C. H.; Pascal, T.; Teran, A. A.; Marcus, M. A.; Cabana, J.; Guo, J.; Prendergast, D.; Salmeron, M.; Balsara, N. P., Fingerprinting Lithium-Sulfur Battery Reaction Products by X-ray Absorption Spectroscopy. *J. Electrochem. Soc.*, **2014**, 161, A1100 - A1106.
7.   Cuisinier, M.; Cabelguen, P. E.; Adams, B. D.; Garsuch, A.; Balasubramanian, M.; Nazar, L. F., Unique behaviour of nonsolvents for polysulphides in lithium–sulphur batteries. *Energy Environ. Sci.*, **2014**, 7, 2697 - 2705.
8.   Dominko, R.; Patel, M. U. M.; Lapornik, V.; Vizintin, A.; Koželj, M.; Tušar, N. N.; Arčon, I.; Stievano, L.; Aquilanti, G., Analytical Detection of Polysulfides in the Presence of Adsorption Additives by Operando X-ray Absorption Spectroscopy. *J. Phys. Chem. C*, **2015**, 119, 19001 - 19010.
9.   Gorlin, Y.; Siebel, A.; Piana, M.; Huthwelker, T.; Jha, H.; Monsch, G.; Kraus, F.; Gasteiger, H. A.; Tromp, M., Electrolyte System for High Voltage Li-Ion Cells. *J. Electrochem. Soc.*, **2015**, 162, A1146 - A1155.
10.   Cuisinier, M.; Hart, C.; Balasubramanian, M.; Garsuch, A.; Nazar, L. F., Radical or not Radical: Revisiting Lithium-Sulfur Electrochemistry in Non-Aqueous Electrolytes. *Adv. Energy Mater.*, **2015**, 5, 1401801 - 1401807.
11.   Vijayakumar, M.; Govind, N.; Walter, E.; Burton, S. D.; Shukla, A.; Devaraj, A.; Xiao, J.; Liu, J.; Wang, C., Karim A.; Thevuthasan, S., Molecular structure and stability of dissolved lithium polysulfide species. *Phys. Chem. Chem. Phys.*, **2014**, 16, 10923 - 10932.
12   Lu, Y.-C.; He, Q.; Gasteiger, H. A., Probing the Lithium–Sulfur Redox Reactions: A Rotating-Ring Disk Electrode Study. *J. Phys. Chem. C*, **2014**, 118, 5733 - 5741.
13.   Kumar, P.; Nagarajan, R.; Sarangi, R., Quantitative X-ray absorption and emission spectroscopies: electronic structure elucidation of Cu_2S and CuS. *J. Mater. Chem. C*, **2013**, 1, 2448 - 2454.